On the Use of Process Analytical Technologies and Population Balance Equations for the Estimation of Crystallization Kinetics. A Case Study

Nesrine Gherras
Ecole des Mines de Saint Etienne, Centre SPIN, LPMG, UMR CNRS 5148, 158, cours Fauriel, 42000 Saint Etienne, France

Gilles Fevotte
Ecole des Mines de Saint Etienne, Centre SPIN, LPMG, UMR CNRS 5148, 158, cours Fauriel, 42000 Saint Etienne, France

Université de Lyon, Université Lyon 1, 43 bld du 11 Novembre 1918, 69100 Villeurbanne, France

DOI 10.1002/aic.12776
Published online October 24, 2011 in Wiley Online Library (wileyonlinelibrary.com).

The batch cooling solution crystallization of ammonium oxalate was performed in water at various constant cooling rates. Measurements of the solute concentration were obtained using in situ attenuated total reflectance fourier transform infrared (ATR-FTIR) spectroscopy, and final estimates of the crystal size distribution (CSD) were computed; thanks to in situ image acquisition and off-line image analysis. The crystallization process was then simulated using population balance equations (PBEs). Estimates of the nucleation and the growth parameters were computed through model/experiments fitting. According to the cooling rate, the PBE model allowed distinguishing between two distinct crystallization regimes, separated by an "intermediate regime." The respective contributions and shortcomings of solute concentration measurements and granulometric data to the identification of nucleation and growth kinetic parameters are analyzed and discussed. It is shown in particular that no real separate estimation of nucleation and growth parameters can be obtained in the absence of CSD data. © 2011 American Institute of Chemical Engineers *AIChE J,* 58: 2650–2664, 2012
Keywords: crystal growth (industrial crystallization), design (process simulation), nucleation, process control, particle/count/measurements

Introduction

Batch crystallization is extensively used in chemical and pharmaceutical industry as a separation and purification process, especially when small-scale production of high value-added chemicals is concerned. The control of batch crystallization process is essentially intended to improve the crystal size distribution (CSD) with respect to the processing properties of the particles, the purity of final crystals, and the crystal habit and morphology. Indeed, controlling these properties remains an important industrial issue since most particle features influence the ease of processing of the particulte product (e.g., flowability, filterability, caking, or dusting ability) and many of its quality and end-use properties (e.g., dissolution rates, apparent density, hardness, specific area, etc.). To a large extent, these latter properties, for example, the defect content (e.g., structure dislocation, solvent occlusions, etc.) and the chemical purity, also depend on the bulk properties of the solid. Consequently, there is a clear need to better understand how operating parameters like solvent composition, supersaturation and temperature profiles, concentration of impurities, hydrodynamics, etc. can affect the final product properties.

Appropriate dynamic models describing industrial crystallization processes are expected to allow analyzing and understanding the advancement of basic crystallization phenomena (e.g., nucleation and growth) and therefore to develop improved operating strategies. The goal of these strategies is of course to enhance both the quality of the final product and the productivity of the batch operations in question. Many significant examples of this kind of approach were reported recently.[1–6] Among other topics, the article raise two major questions:

(1) As far as process development is concerned, how about estimating reliable nucleation and growth kinetic parameters?

(2) How can advanced dynamic crystallization models be used for targeting desired final CSDs?

For two different aqueous systems (paracetamol and potassium dichromate), the aforementioned articles demonstrate the possibility of designing seeding strategies that enabled prespecified multimodal CSDs to be obtained. A key to such

Correspondence concerning this article should be addressed to G. Fevotte at fevotte@emse.fr.

innovative experimental applications is the joint use of advanced mathematical and numerical tools for modeling the distributed systems involved (i.e., population balance equations, PBEs) together with efficient process analytical technologies (PATs) offering powerful means of monitoring the dynamic behavior of the same processes. Compared with such articles, the present work does not deal with process control; it is rather intended to shed some light on important aspects of the estimation of crystallization kinetic parameters. Nagy et al.[3] compared the performances of "standard metastable zone width (MSZW) methods" with the efficiency of a method based on a simplified dynamic model of the crystallization process. The modeling approach combines PBEs, concentration measurements using ATR-FTIR spectroscopy, and particle size distribution measurements using focused beam reflectance measurements (FBRMs). As one could expect, the latter method is much more efficient and reliable in estimating nucleation and growth parameters.

This article reports results of a study of the cooling solution crystallization of ammonium oxalate (AO) in water. It follows a previous article comparing four versions of "classical" simplified approaches of MSZW or induction time measurements.[7] The rough assumptions made with these methods were shown to allow some predictions of the onset of detectable nucleation (which should not be mixed up with the onset of primary nucleation). However, no reliable prediction of the number of particles generated when the limit curve of metastable zone is reached could be made using these methods.

This second article addresses again on the problem of kinetic parameter estimation. ATR-FTIR measurements of concentration and infrequent CSD data are now used for estimation purposes. The CSD data were acquired using in situ image acquisition. The objective is to estimate possible concomitant and/or successive nucleation mechanisms. In the particular case of the crystallization of AO in water, it is shown that difficulties can be raised by changes in the crystallization mechanisms, depending on the operating conditions (the cooling rate in the present case).

In fact, during the last 15 years, the significant development of in situ online measurement techniques for monitoring crystallization processes allowed many progresses regarding the control of both the quality and reproducibility of particulate products.[8–10] In the field of pharmaceutical development and production, the "PAT" initiative of the FDA [8,11] is a good illustration of the expectations and successes associated to a better control of industrial crystallizers. From a more academic point of view, continuous and in situ measurement tools made it possible to obtain refined experimental results and allowed advanced modeling and control approaches to be developed. Former approaches were usually based on infrequent off-line suspension samples, but sampling and analyzing crystallizing suspensions remains a complex and poorly reliable process, which is also limited by the restricted number of possible measurements.

Many innovative applications of PATs to crystallization processes for the development of advanced monitoring, modeling, and control strategies are reported in the literature. From an industrial point of view, mastering the final CSD is clearly a major issue, which has been the subject of many studies in the past. Supersaturation control, nucleation, and/or dissolution control studies constitute the major part of this kind of applications which, in turn, are mostly based on optimal or pseudo-optimal temperature tracking. As an example of recent innovative studies, Aamir et al.[2] demonstrate experimentally the possibility of targeting desired final CSD through the design of optimal seed parameters. Indeed, as far as designing kinetic crystallization models are concerned, many parameters have to be identified. Unfortunately, the relevance and the significance of parameter estimation techniques in the mathematical framework of highly nonlinear, nonstationary, and strongly coupled phenomena such as nucleation, crystal growth, or agglomeration remain questionable. Few studies were actually devoted to this question (see, e.g., Refs. [12–14]). Despite the importance of the problem of parameter sensitivity and "identifiability," many authors still have recourse to old and relatively rough methods for estimating nucleation parameters, which theoretical bases are questionable. For example, measurements of induction times and MSZW aiming at evaluating the kinetics of nucleation remain largely practiced in the crystallization engineering community.[15–17] It therefore seems very important to raise the following question: as far as in line sensors are now made available for kinetic parameters identification purposes, what is exactly the necessary information for appropriate crystallization kinetic parameter estimation? In particular, is it essential to have available measurements of both liquid and dispersed solid phases in presence? This article is intended to bring some answers to these questions related to the design of relevant measurement strategies.

AO monohydrate dissolved in water was selected here as a model-system. Previous workers have thoroughly investigated the crystallization of AO.[18–20] The mechanisms and kinetics of crystal growth and nucleation were studied, and the effect of some cationic impurities on the nucleation and growth processes was also investigated.[21–24] However, the published models are derived from specific experiments assuming that crystal nucleation and crystal growth do not occur simultaneously. The corresponding rates are usually estimated from single crystals experiments at fixed temperature and/or constant supersaturation,[19] which lead to strongly limiting constraints. Moreover, in many cases, the nucleation parameters are characterized from induction time or MSZW measurement methods.[18,25] Because of their simplicity and to the very restrictive hypotheses made, these latter methods present weaknesses and approximations which justify their call into question.

Through the batch cooling solution crystallization of AO experiments performed at different cooling rates, this work is focused on the development of experimental and numerical protocols for estimating nucleation and growth kinetics, as well as on the development of suitable models for process development and optimization purposes. During this study, in situ image acquisition and ATR-FTIR spectroscopy were used for real-time process monitoring. Models describing the dynamic behavior of the crystallization process were designed, thanks to the mathematical framework of PBEs. The nucleation and growth kinetic parameters were then estimated using "standard" nonlinear numerical optimization techniques (i.e., through the minimization of quadratic criteria quantifying the difference between the experimental data and the model-predicted ones).

PBEs

Crystal growth rate

PBEs are widely used as a modeling framework in the engineering of dispersed media, with applications including crystallization, powder technologies, polymerization processes, biotechnologies, etc.[26–29] In most published

crystallization, PBE modeling works on the crystal growth rate G, which is assumed not to depend on the particle size (McCabe's hypothesis) but essentially on supersaturation. Several expressions of supersaturation may be defined, according to the theoretical background of the study. The following equations define both the relative supersaturation $\sigma(t)$ and the supersaturation ratio $\beta(t)$, which both are dimensionless variables used in kinetic models

$$\sigma(t) = \frac{C(t) - C^*(T)}{C^*(T)} \tag{1}$$

$$\beta(t) = \frac{C(t)}{C^*(T)} \tag{2}$$

The following expression can also be used as an expression of the crystallization driving force

$$\Delta C(t) = C(t) - C^*(T) \tag{3}$$

where C^* is the equilibrium concentration (i.e., the solubility of the solid crystallizing compound in a given solvent) and $C(t)$ is the solute concentration.

The growth of crystals from solution is a complex process. Depending on the solute-solvent system in question, many steps may be involved during the crystal growth (e.g., bulk and surface diffusion, solvation, integration, etc) and this is the reason why "standard" models used to represent the growth process are more or less comprehensive and approximate.[30–32] The crystal growth rate is usually approximated as the rate at which a specific or an average characteristic size L of crystals increases

$$G(t) = \frac{dL}{dt} \tag{4}$$

Many expressions of the crystal growth rate were formulated. For example, the celebrated Burton, Cabrera, and Franck (BCF) screw dislocation model was proposed in 1951.[33] The following expression can be used to represent various growth mechanisms, according to appropriate parameters c and D

$$G_{\mathrm{BCF}}(t) = \frac{dL}{dt} = c\frac{(\beta(t)-1)^2}{D}\tanh\left[\frac{D}{\beta(t)-1}\right] \tag{5}$$

The BCF model roughly corresponds to the following orders of supersaturation dependency

$$G \propto \sigma^2 \ \text{ for low values of } \sigma \text{ and } \ \exists\sigma_c \text{ with } \ G \propto \sigma \ \text{ for } \sigma > \sigma_c \tag{6}$$

Experimental results describing the linear growth rates of AO monohydrate [$(NH_4)_2C_2O_4{\cdot}H_2O$; AO] crystals were previously published by Mielniczek-Brzóska and Sangwal.[31] The crystals were grown through constant-temperature or constant-supersaturation processes at 30 and 40°C in the supersaturation range of 1–9%. The supersaturation dependence of the growth rate was found to obey a parabolic law, which roughly speaking is consistent with model (5) for low supersaturation values.

First principle models like Eq. 5 should not necessarily be used when dealing with process engineering studies. Because of their simplicity and to the limited number of parameters involved, basic phenomenological models are currently applied despite their lack of physical meaning. Such models usually assume power supersaturation dependency like the following

$$G(t) = k_{\mathrm{g}}\sigma(t)^j \tag{7}$$

where exponent j is likely to depend on the involved growth mechanism(s) and, in particular, on the level of supersaturation. In practice, consistently with current theoretical models, most published values of j are given between 1 and 2 and k_{g} is a temperature-dependent growth parameter.

Crystal nucleation rate

Many primary and secondary nucleation models are available in the literature. The following expression of primary homogeneous nucleation is derived from the classical nucleation theory (CNT). This latter model will be used in the sequel to simulate primary homogeneous nucleation occurring during batch unseeded cooling crystallization of AO

$$R_{N_1}(t) = A_{\mathrm{hom}}\exp\left[\frac{-B_{\mathrm{hom}}}{T^3(Ln\beta)^2}\right] \tag{8}$$

Theoretical expressions of parameters A and B can be found in the literature.[34,35] The following expressions are typically used, according to the mechanism involved

$$B_{\mathrm{hom}} = \frac{16\pi v_0^2\gamma^3}{3(kT)^3} \tag{9}$$

$$A_{\mathrm{hom},D} = \mathcal{D}\left[\frac{kT}{v_0^2\gamma}\right]^{1/2}\mathcal{N}_A\mathrm{C}^*\ \ln\beta \tag{10}$$

Equation 10 corresponds to diffusion controlled nucleation, whereas the following expression is used to describe nucleation controlled by interface transfer

$$A_{\mathrm{hom},I} = \mathcal{D}\left[\frac{\gamma}{kT}\right]^{1/2}\left[\frac{4\pi}{3v_0}\right]^{1/3}\mathcal{N}_A\mathrm{C}^* \tag{11}$$

When heterogeneous nucleation is the predominant mechanism, parameter B is given by the following expression

$$B_{\mathrm{het}} = \mathcal{D}\frac{16\pi\ v_0^2\ \gamma_{\mathrm{eff}}^3}{3(kT)^3} \tag{12}$$

where T is the absolute temperature (K), $\mathcal{D}$ is the diffusivity of the solute (m^2/s^{-1}), v_0 is the solute molecular volume, γ is the crystal-liquid interfacial energy (J/m^2), and k is the Boltzmann constant (J/K^1).

Expressions (9) and (12) differ in the value of the interfacial energy: when heterogeneous nucleation takes place, γ is then replaced by γ_{eff}, which is usually significantly smaller.

Secondary nucleation is also likely to take place during the crystallization of AO. This latter mechanism is usually considered to be promoted by increasing amounts of solid in suspension, even though numerous phenomena can be referred to as secondary nucleation (initial breeding, attrition, etc.). These phenomena were the object of intense researches during the past decades.[34–36] Many knowledge-based models were proposed that cannot always easily be identified and which are likely to occur simultaneously. For the sake of simplicity, secondary nucleation phenomena are represented below using a phenomenological kinetic equation accounting

for the dependence of the secondary nucleation process upon the supersaturation, the energy dispersed through stirring ε_a, and the concentration of solid in suspension $C_s(t)$

$$R_{N_2}(t) = A_{SN}\, C_s(t)^k\, \sigma(t)^{\,i}\, \varepsilon_a^n \tag{13}$$

For the sake of simplicity, parameter A_{SN} is considered constant in the range of experimental temperature used in this study. Values of exponent k and i are expected between 0 and 2. The input agitation power will not be considered in this work because the stirring rate was kept constant during the experiments.

Monodimensional PBEs modeling of the cooling crystallization process

Supersaturation is the driving force of crystallization. Computing $\beta(t)$ requires measurements of the solute concentration $C(t)$ during the crystallization process. Actually, the decrease of $C(t)$ is caused by the generation of crystals as the molecules of solute initially present in the liquid phase are transferred through crystallization to the dispersed solid phase. The total amount of solid can therefore be computed from the total volume of particles computed through the integration of the whole CSD

$$C_s(t) = \frac{\rho_s \varphi_p}{M_s} \int_{L^*}^{\infty} \psi(L,t)\, L^3 dL \cong \frac{\rho_s \varphi_p}{M_s} \int_{0}^{\infty} \psi(L,t)\, L^3 dL \tag{14}$$

where ψ(L,t) is the number population density function of particles with size L, ρ_s (kg/m^3) and M_s are the density and the molecular weight of the solid compound, φ_p is a volumetric particle shape factor (e.g., $\pi/6$ in the ''ideal'' case of spherical crystals).

A mass balance of the solute consumption allows computing $C(t)$ at each time step and consequently yields $\sigma(t)$ through Eq. 1, provided that experimental data about the solubility curve $C^*(T)$ are available. In the following, the crystallization is assumed to take place in a perfectly mixed batch reactor and crystals are assumed to be generated through nucleation phenomena only. According to the classical nucleation theory (CNT), the size of initial particles generated in the dispersed phase is the critical size L^* which is neglected in the following (i.e., from a purely numerical viewpoint). Moreover, for the sake of simplicity, agglomeration or breakage processes are neglected in the sequel. According to Eq. 14, the amount of solid generated though the crystallization of particles depends on the size, but also on the shape which is approximately described by the shape factor φ_p. Knowledge of the shape factor obviously determines the consistency between the concentration trajectory $C(t)$ and the time variations of the CSD. Now, as outlined below, it is clear that 2D image analysis allows measuring two main sizes (i.e., the length, L and the width, W) in a rather reductive way, not only because the ratio L/W is actually randomly distributed and evolves during the batch process as a function of L(t) but also because measuring L is not really straightforward. According to their space-orientation in the video measurement cell, the AO anisotropic particles exhibit unpredictable apparent length L_a such that, obviously, $L_a \leq L$. Using an average shape factor can improve the ability of φ_p to relate the volume of solid, but such a correction will by no means account for other random effects such as the apparent size reduction resulting from the projection of 2D images of the real crystals. It was not the goal of this study to investigate more deeply the way of computing reliable size data from 2D image analysis. As outlined in the following, the accuracy of the estimated experimental CSDs used for the identification procedure remain rather poor, but despite their limitations, these data were undeniably valuable for successful parameter estimation procedure. An average value of the shape factor was evaluated from video pictures taken during experiments randomly selected in the whole range of cooling conditions. More than 1500 particles of different sizes were used for the calculation of the average shape factor. Assuming that the particles are parallelipipedic with square basis, the width w of the square section was evaluated to be roughly equal to $L/5$, where L was assumed to be the length defined by Eq. 4. φ_p was therefore set to 1/25 in PBE model.

Perfect mixing of the suspension implies that the number density function does not depend on external space coordinates. The following boundary conditions link the nucleation rate(s) of crystals to the overall particle number. In the case of monodimensional particles, the previous assumptions lead to the PDE (15) describing the time variations of the CSD, where $\psi(L,t)$ is the number population density function (PDF) of crystals of size L, at time t

$$\frac{\partial \psi(L,t)}{\partial t} + G(t)\frac{\partial \psi(L,t)}{\partial L} = 0 \tag{15}$$

$$\psi(L,0) = 0 \tag{16}$$

$$\psi(0,t) \approx \psi(L^*,t) \approx \frac{R_N(t)}{G(t)} \tag{17}$$

$R_N(t)$ is the overall rate of nucleation expressed in # s^{-1} m^{-3} (i.e., the sum of primary and secondary nucleation phenomena).

A simplified method of characteristics (MOCs) was applied during the study to solve numerically the PBEs.[37] Indeed, the low computation time of the MOC appeared suitable with further applications of nonlinear optimization techniques to the estimation of kinetic parameters.

Identification of the kinetic parameters of the crystallization process

It is obvious that, as far as quantitative kinetic crystallization studies are concerned, the experimental data should provide enough information to enable the evaluation of several simultaneous and coupled phenomena. In practice, it is very difficult to ''isolate'' these latter phenomena (i.e., to make specific observations of every single phenomenon such as homogeneous or heterogeneous nucleation and growth), or at least to separate their respective contribution to the overall crystallization process. An example of this difficulty is given below where it is shown that even accurate measurements of the time variations of solute concentration do not allow estimating the nucleation rate. This shortcoming arises from the fact that experimental CSD data are essential to make the distinction between nucleation and growth effects in the overall solute consumption.

Now, assuming that appropriate data describing both the dispersed and the continuous phase are available, estimates of the parameter values can be obtained through the minimization of the quadratic error between experimental data and model predictions. The optimization procedure used in the

Table 1. Optimal Nucleation and Growth Kinetic Parameters: Observation of Two Different Crystallization Regimes, Depending on the Cooling Rate

Equations: Crystallization Regime (Depending on dT/dt)		(8)		(13)			(7)		
		A_{hom} (#.m^{-3}/s^{1})	B_{hom} (−)	A_{SN}	i	k	k_g (s/m^{-1})	j	Nucleation Mechanism
1.1	R_1[†] ($dT/dt \geq -12$°C/h)	5.05×10^6	3.83×10^6	–	–	0	2×10^{-5}[‡]	1	R_{N_1}
1.2	R_2[†] ($dT/dt \leq -20$°C/h)	2.9×10^4	2.78×10^6	–	–	0	2×10^{-5}([‡])	1	R_{N_1}
2.1	R_1[§] ($dT/dt \geq -12$°C/h)	3.52×10^7	4.11×10^6	1.41×10^9	1.36	1.86	2.56×10^{-5}	1	$R_{N_1} + R_{N_2}$
2.2	R_2[§] ($dT/dt \leq -20$°C/h)	6.7×10^7	7.05×10^6	1.40×10^9	1.36	1.77	2.74×10^{-5}	1	$R_{N_1} + R_{N_2}$
Confidence intervals (95%):									
	R_1	$\pm 0.83 \times 10^7$ ($\pm$ 23.6%)	$\pm 0.1 \times 10^6$ ($\pm$ 2.4%)	$\pm 2.3 \times 10^9$ ($\pm$ 16.3%)	± 0.15 ($\pm$ 11%)	± 0.07 ($\pm$ 3.8%)	$\pm 0.23 \times 10^{-5}$ ($\pm$ 9%)		
	R_2	$\pm 1.41 \times 10^7$ ($\pm$ 18.7%)	$\pm 0.11 \times 10^6$ ($\pm$ 1.5%)	$\pm 8.4 \times 10^9$ ($\pm$ 60%)	$\pm 0.11 \pm$ (6.2%)	± 0.067 ($\pm$ 3.7%)	$\pm 0.71 \times 10^{-5}$ ($\pm$ 6.7%)		

The experimental results were not found to be reproducible in the intermediate region (i.e., for -12°C/h $> dT/dt > -20$°C/h). The experimental solute concentration profile was fitted to the simulated one.
[†]Estimations performed using concentration measurements only.
[‡]The growth rate constant was fixed to $k_g = 2 \times 10^{-5}$ m/s such that the final maximum particle size was consistent with real crystals (i.e., between about 1 and 4 mm, depending on the cooling rate).
[§]Estimations performed using both concentration and granulometric data.

following is based on the following weighted non linear quadratic criterion

$$J(t, n, \underline{\theta}) = \min \left(\sum_{n=1}^{N_{exp}} \left[\frac{1}{t_{n,end}} \int_{t=0}^{t_{n,end}} \left[\tilde{C}_n(t, \underline{\theta}) - \hat{C}_n(t) \right]^2 dt + \lambda \sum_{k=0}^{k_{max}} \left[\tilde{\varphi}_k(L_k, \underline{\theta}) - \hat{\varphi}_k(L_k) \right]^2 \right] \right) \quad (18)$$

$$\text{with } \underline{\theta_1} = \left[k_g,\ j,\ A_{hom},\ B_{hom} \right] \quad \text{or} \quad \underline{\theta_2} = \left[k_g,\ A_{hom},\ B_{hom}, A_{SN}, i\ ,\ k \right] \quad (19)$$

where $n \in [0, N_{exp}]$ is the index of one given experiment used for the estimation of the vector of parameters θ (N_{exp} experiments are gathered in the estimation procedure); $t_{n,end}$ is the duration of the nth experiment; k is the index of a given class of particle size ($k \in [0, k_{max}]$); φ_k is the number of particles belonging to the class of average size L_k and λ is a weighting factor introduced to balance the influence of the two variables (i.e., the ''almost continuous'' concentration profile and the discretized size distribution histograms) determining the final optimal value of $J(\theta)$. In practice, λ was set empirically such that a posteriori plots of the model/experiments supersaturation and final CSD profiles appeared satisfactory. Moreover, notations ^ and ˜ refer to the measured and model-predicted variables, respectively.

The optimization problem was solved using *fmincon* from the MATLAB® optimization toolbox. Equation 19 indicates that two parameter vectors were successively submitted to the identification procedure, depending on the experimental complexity of the nucleation process. As explained in the following (see also Table 1), $\underline{\theta_1}$ corresponds to parameter estimations performed when solute concentration measurements were only used as experimental data. In this case, the basic primary nucleation mechanism described by Eq. 8 enabled a very accurate simulation of the measured solute concentration. Nevertheless, as shown below, the predicted particle sizes were significantly underestimated.

The enlarged parameter vector $\underline{\theta_2}$ accounts for secondary nucleation mechanisms and was used when CSD data were included in the experimental data set. As outlined in the following, secondary nucleation appeared to be the only way of reproducing the CSD reconstructed from final in situ image analysis. Parameters A_{SN}, i, and k are defined by Eq. 13. In the same equation, the contribution of stirring to the secondary nucleation process was not involved because the stirring rate was kept constant.

Experimental

Materials

AO monohydrate particles were used in the crystallization experiments. AO was available from Acros Organics with a purity level of 99+%. The crystallized product was used as received, without further purification. Distilled, deionized, and degassed water was used as solvent.

Batch crystallizer set up and in situ characterization techniques

A 3-L glass vessel equipped with a jacket and a condenser was used for the experiments. Stainless-steel baffles and a high efficiency propeller (Mixel TT TM) were set to maintain a good homogeneity of particles in the slurry. The bench-scale plant was instrumented and computer-controlled to allow tracking set-point temperature trajectories. Cooling was performed by means of heat transfer through the jacket wall: the temperature was controlled by manipulating automatically the set-point temperature of a heating bath containing water and glycol with an accuracy of ± 0.5°C. The jacket is baffled and equipped with a pump forcing the circulation to improve the heat transfer capacity. All experiments were performed with constant cooling rates and terminated by a isothermal period at 20°C.

In situ concentration measurements were performed using the infrared spectrometer ''MATRIX-F'' manufactured by Brucker Optik GmbH, equipped with ATR-diamond immersion probe (diamond prism with two reflexion angles of 45°). The ATR probe was connected to the spectrometer

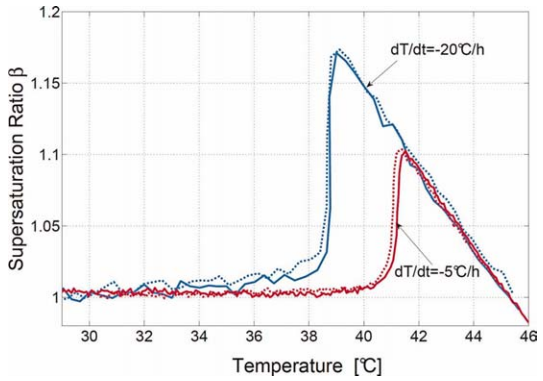

Figure 1. Example of supersaturation profiles measured during AO crystallization in water performed at two cooling rates (−7 and −20°C/h).

The two sets of two runs show the reproducibility of the process and of the ATR-FTIR measurements. [Color figure can be viewed in the online issue, which is available at wileyonlinelibrary.com.]

through an optical fiber. The measurement cell, the optical conduit, and the probe were purged using nitrogen to avoid irreproducible spectra due to the sensitivity of the measurements to the time variations of the concentration of water and carbon dioxide in the ambient air. The source of light was a polychromatic laser emitting in mid-IR. The detection was performed by a MCT detector cooled with liquid nitrogen. The resolution of the detection was set to 4 cm^{-1}. The acquisition of the IR spectra was performed with a sampling period of 30 s during which the calculation of an average spectrum was obtained from 32 scans. The principle of the concentration ATR FTIR measurements will therefore not be recalled here: the calibration procedure was widely published in the past.[38–42] After validation, the calibration model was used to evaluate the time variations of supersaturation; as displayed in Figure 1 the reproducibility of the measurements was satisfactory. The solubility curve displayed in Figures 4–6 was obtained using continuous ATR-FTIR measurements. As already reported[43]: thanks to slow cooling and heating of AO suspensions, very low levels of super- and under-saturation can be covered such that the two measured curves can be made as close as possible. The unique curve finally obtained or the average of the two curves was then assumed to fit the solubility.[7]

In addition to the in situ FTIR measurement of solute concentration, the CSD of the final product was evaluated through image analysis. The "EZProbe,"[44] an in situ imaging probe developed at the University of Lyon was used for the video monitoring of the crystallizing slurry. The imaging probe allowed real time acquisition of 2D images of AO particles during the batch process, as shown in Figure 2. Size measurements were performed for each discernible crystal with a minimum sample of 900 crystals per CSD analysis. Because of the time required by the processing of the video pictures, only final size distributions were actually computed for each experiment.

It is clear that obtaining in situ CSD measurements is of tremendous interest for monitoring crystallization operations as well as for process development and control purposes. This is why a significant research effort is actually devoted to the development of 2D and 3D strategies that would enable the reconstruction of CSDs from in situ video pictures.[45–47] However, measuring the CSD though image processing is not an easy task. Several reviews of the most challenging problems raised by in situ image analysis can be found in the literature.[48,49] In fact, many problems remain unsolved which are notably due to the difficulty of differentiating overlapping or fuzzy particles, even for slightly dense suspensions (say, for solids content below 6–8%). The anisotropy of particles also induces significant uncertainties as the apparent sizes depending on the projected crystal faces and, consequently, on the space orientation of the particles. The range of measurable particles is also limited. In particular, three main size effects should be outlined: (1) The biggest crystals are more likely than the small ones to stick out from the frame of the picture so that their number is unavoidably underestimated; (2) because of the limited optical and numerical resolution of the images, crystals with size smaller that 5 μm cannot be distinguished, and crystals between about 5 and 10 μm are very difficult to characterize; (3) as a general rule, small crystals are likely to be masked by bigger ones so that, again, their number is underestimated.

It is not the goal of this study to deal with the many difficulties arising from the measurement of particle sizes through image analysis. Several applications were reported by the group, which were only claimed to bring partial and imperfect solutions applicable for monitoring specific particulate systems: the automatic monitoring of the crystallization of rather spherical but fuzzy particles[42,44] and the automatic monitoring of anisotropic crystals.[50] In the following, the processing of suspension pictures were performed for low solid contents using the image processing algorithm proposed by Ahmad et al.[50] When the automatic procedure was found to be inefficient because of excessive solid contents, the results were corrected through manual operations. More comments about the limitations of the CSD measurements of AO particles will be made in the following.

Experimental procedure for linear batch cooling experiments

For the sake of industrial applicability, the experimental design was focused on the joint investigation of the

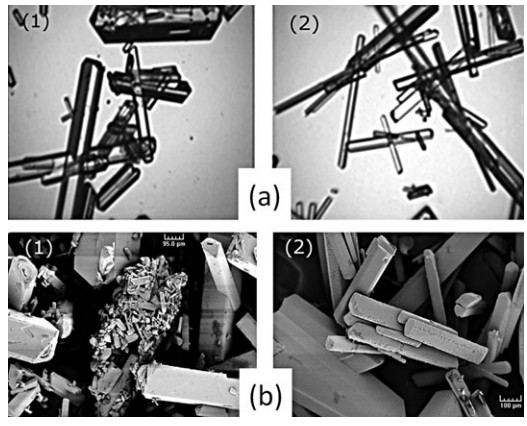

Figure 2. (a) Typical pictures of AO crystals acquired using the in situ video probe during batch experiments performed with two different cooling rates: (1) "low" cooling rate: *dT/dt* = −10°C/h and (2) higher cooling rate: *dT/dt* = −25°C/h.

(b) SEM pictures of crystals withdrawn at the end of the batch cooling process.

nucleation and growth kinetics of AO monohydrate during batch cooling runs. Indeed, one cannot reasonably expect industrialists to investigate crystallization systems through "academic" laboratory experiments (e.g., using specific growth-cells operated in such a way that nucleation can be neglected). This is why estimating the whole set of kinetic crystallization parameters through "usual" batch experiments appears as an attractive objective. However, a major objection to such an approach lies in the fact that many industrial crystallization operations often exhibit unpredictable behavior. This is particularly true for the onset of primary nucleation. Erratic onset of nucleation explains why seeding is generally assumed to be way of circumventing the nonstationary features of crystallization systems. Fortunately, with the present system the reproducibility of unseeded batch experiments was satisfactory and allowed acquiring reproducible experimental data. For example, it can be seen in Figure 1, that the onset of primary nucleation was reproducible.

AO undersaturated solutions were prepared by dissolving analytical grade AO monohydrate in 1800-mL water. The initial AO concentration ($C_0 \approx 0.1$ kg/kg solvent) was measured accurately. To ensure complete dissolution, the suspensions were heated several degrees higher than the saturation temperature (323 K) and maintained for at least 2 h at this temperature. The completion of the dissolution was checked using both ATR-FTIR and image acquisition. Linear cooling experiments were then performed at varying constant cooling rates, namely: $R = -dT/dt = 2$, 5, 7, 10, 12, 20, 25, and 30°C/h. For the sake of repeatability, at least three experiments were performed for each cooling rate. Cooling was stopped at 293 K and followed by a period of stabilization of 3 h at this latter temperature. Suspension samples were then withdrawn at 293 K, filtered off and dried for optical microscopy and SEM investigation.

Parameter Estimation and Simulation Results

Some questions about estimating crystallization parameters using concentration measurements only

The relevancy of studies devoted to the kinetic estimation and modeling of crystallization processes when no CSD data is made available (i.e., even average or partial experimental data about the dispersed phase) are now questioned. As expected, Figure 1 shows that increasing cooling rates widen the apparent MSZW and increase the maximum relative supersaturation (see also Figure 5). Is it realistic to expect any relevant estimation of both nucleation and growth kinetic parameters from solute concentration measurements only? A priori, it does not seem reasonable to base the characterization of the many coupled phenomena involved during the crystallization process on concentration measurements only because such experimental information does not provide quantitative data about the number of particles. It can be argued, for example, that many slowly growing particles (high nucleation rate can occur together with slow growth rate) could lead to the same solid consumption as few rapidly growing crystals. Consequently, identical concentration trajectories could be reproduced using different sets of kinetic parameters and yield different final simulated CSD profiles.

On the other hand, there exists a one-to-one relationship between the $[T(t), C(t)]$ point where the concentration starts to decrease during a given batch cooling process (i.e., this point is usually referred to as the "limit of metastable zone"), and the value of parameter B_{hom}. In other words, the onset of significant primary nucleation burst can only be reproduced, thanks to a single value of B_{hom}. As shown below, it was observed that the "best" PBE simulation of the experimental concentration trajectory was obtained with parameters predicting excessively small particle sizes. To illustrate this point, Figure 3a displays an exact fit of measured and simulated solute concentration profiles for a batch experiment performed with a cooling rate $dT/dt = -7$°C/h. It appears clearly that the simulation reproduces unrealistic final particle sizes of the order of 10–20 μm: in Figure 3d the final average particle size is 10 μm while it was experimentally observed to be of the order of several hundreds of micrometer.

Actually, there exists an infinity of "pseudo-optimal" binomials (A_{hom}, k_g) leading to the exact representation of a given experimental supersaturation profile. This fact is illustrated in Figure 4 where simulation results are displayed for three different values of parameter A_{hom}. It appears that setting any value of A_{hom} is compatible with the exact fit of solute experimental concentration profiles. Three perfectly superimposed simulated and experimental $C(t)$ curves are displayed in Figure 4a where decreasing values of A_{hom} are combined with increasing values of the growth rate constant k_g (curves 1 till 3 in Figure 4)

To shed some light on the relationship between A_{hom} and k_g, Appendix shows that when the crystallization process is assumed to be initiated through primary nucleation only, an "exact" fit of the measured concentration trajectory is obtained for a single product $A_{hom}\ k_g^3$, whatever the value of A_{hom}. This implies that without additional information on the real distribution of particles sizes, nucleation and growth kinetics remain so closely "intricate" that they cannot be separated. The solute concentration data does not "contain" enough information about the mechanisms responsible for the generation of new particles over time, and information about the "true" particle size is therefore essential. The optimization results presented in Figure 4 strengthen and clarify this idea that no identification of both A_{hom} and k_g is possible without CSD data. As far as induction time techniques are concerned, it follows that as these methods do not account for any explicit information about the growth rate or the time variations of the CSD (except very vague assumptions about the amount and/or the size of solid particles observed when the metastable zone limit is supposed to be reached) one cannot expect relevant estimation of the nucleation rate to be obtained.

It can also be concluded from Figure 4 and Appendix that during the parameter optimization procedure, setting any a priori erroneous value of parameter k_g will not keep the algorithm to converge towards a single "optimal" value of product $A\ k_g^3$. In the absence of additional experimental information, the "real" value of parameter k_g was arbitrarily set to 2.10^{-5} m/s in the following. $k_g = 2.10^{-5}$ m/s cannot be considered as the best estimate of the growth rate parameter, but is was set such that the final maximum simulated particle sizes roughly correspond to the real crystals.

The previous observations agree with Nagy et al.[3] who showed that nucleation and growth kinetics cannot simultaneously be estimated from simple metastable zone experiments. Actually, unlike MSZW methods[51,52]; the authors[3] showed that the estimated kinetic parameters remain uncertain when the growth rate of crystals is not taken into appropriately account through the use of a dynamic model of the crystallization process. It should also be noted that, whatever

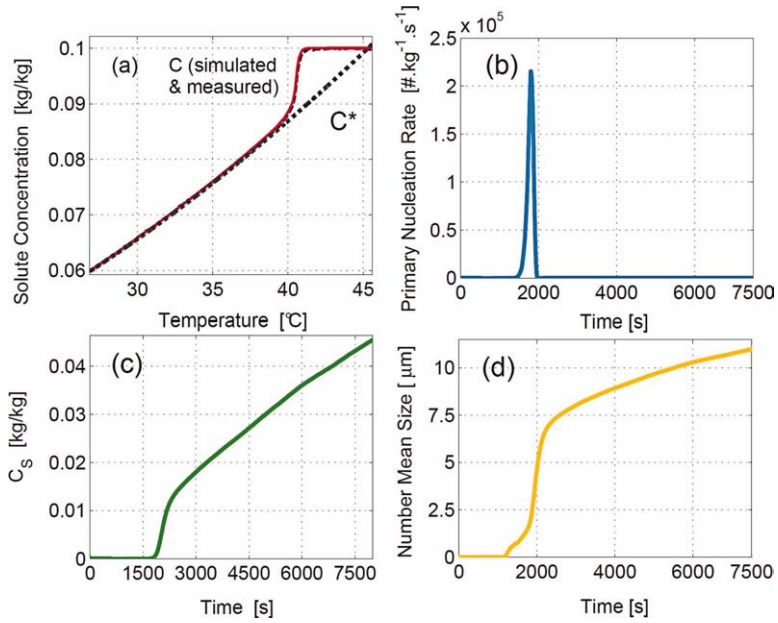

Figure 3. Batch cooling AO crystallization performed with $dT/dt = -7°C/h$.

Simulation of key-process variables using the optimal set of parameters estimated assuming that primary homogeneous nucleation is the only mechanism of particle generation. (a) The simulated and experimental concentration profiles $C(t)$ are almost exactly superimposed (solid line = simulation, dashed line = measured). [Color figure can be viewed in the online issue, which is available at wileyonlinelibrary.com.]

the way of interpreting MSZW or induction time measurements, the boundary condition of Eq. 17 indisputably states that both the nucleation and the growth rate (i.e., the ratio R_N/G) determine the number of generated particles. One cannot therefore reasonably expect any estimation strategy to go without experimental information about the two terms in question.

In this context, this study is also a contribution to many previous experimental studies suggesting the two main following ideas: (1) multiple (in both terms of measured parameters and measurement frequency) and advanced experimental data are essential to the identification of true crystallization kinetic parameters; (2) at least one experimental parameter quantifying the CSD should be made available

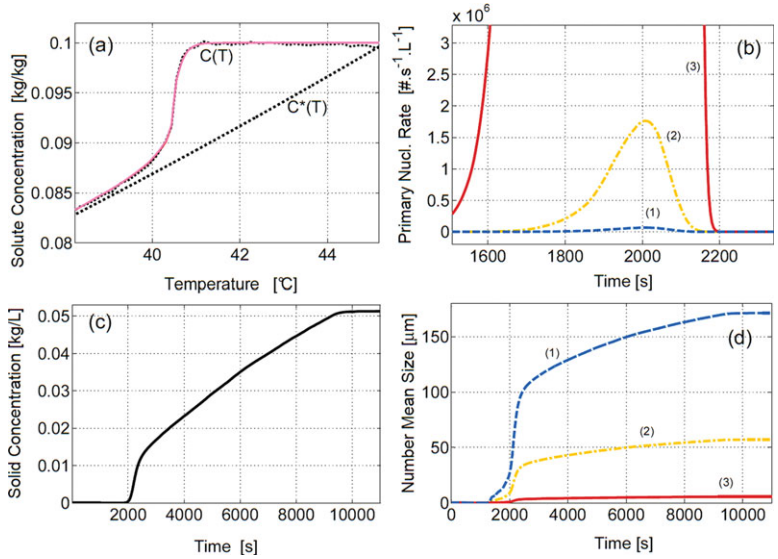

Figure 4. "Optimal" simulation of the concentration profiles during batch cooling operations performed with a cooling rate of −10°C/h.

$B_{hom} = 3.83 \times 10^6$ is constant for the three simulated runs, three values of the growth rate constant are set to $k_{g1} = [4.86 \times 10^{-6}$ m/s $^{(1)}$, $k_{g1}/3$ $^{(2)}$, $k_g = k_{g1}/30$ $^{(3)}]$. A_{hom} is optimized to the simulated solute concentration trajectory to fit the measurements [dotted line in (a)]. [Color figure can be viewed in the online issue, which is available at wileyonlinelibrary.com.]

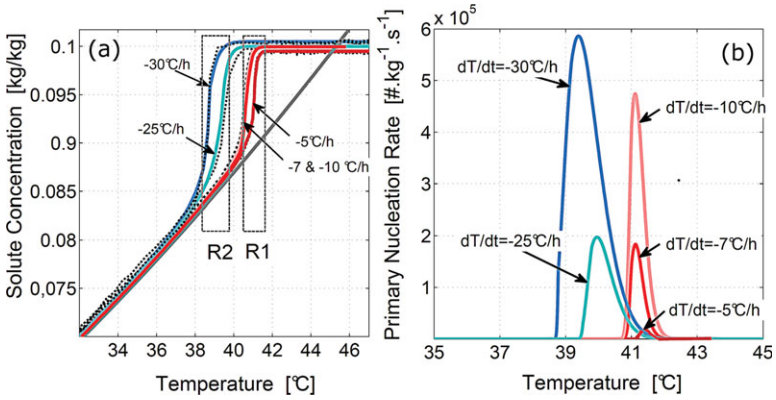

Figure 5. (a) Solubility curve $C^*(T)$ of AO in water measured using in situ ATR-FTIR spectroscopy.

Measured (dashed lines) and simulated (solid lines) solute concentration profiles of batch operations performed with varying cooling rates. (b) Simulation of the primary nucleation rates. Regimes R_1 and R_2 correspond to $dT/dt = -5$, -7, and 10°C/h and $dT/dt = -25$ and -30°C/h, respectively. [Color figure can be viewed in the online issue, which is available at wileyonlinelibrary.com.]

for appropriate estimation of both nucleation and growth kinetics.

Moreover, as far as the particular case of the crystallization of AO in water is concerned, the identification results presented below suggest that the reliability of crystallization parameters estimated from batch-wise experiments should be brought into question when varying operating conditions are dealt with. Indeed, it is shown in the following that the system under investigation exhibits various kinetic behaviors depending on the rate of generating supersaturation.

Crystallization parameter estimation based on experimental solute concentration profiles

Despite the previous pessimistic conclusions about the impossibility of estimating the "true nucleation parameters" in the absence of crystal size data, it is clear however that continuous measurements of the solute concentration provide more valuable information than "standard" MSZW methods. Indeed, in the latter case, the experimental data simply allow "interpreting" the onset of a bifurcation in the solute concentration trajectory which is then interpreted in terms of nucleation rate (i.e., the rather subjective and approximate observation of apparent nucleation burst). Thanks to ATR-FTIR measurements, the available continuous in situ measurements contain much accurate and comprehensive information than MSZW measurements. One can therefore reasonably expect online concentration measurements reported here to allow improved estimation of crystallization kinetic behavior.

To clarify this point, Figure 5 presents the experimental and computed time variations of solute concentration measured during five runs performed with varying cooling rates. The simulated results were obtained as explained earlier. Here, the parameter estimation procedure was based on ATR-FTIR in situ concentration measurements only. At low cooling rates, the simulated concentration profiles fit satisfactorily the experimental data. It should be noted that the phenomenological Eq. 7 did not call for particular refinement. In particular, reproducing the overall dynamics of the process did not require to account for the effect of temperature on the growth kinetic constant k_g. Parameter j relates the effect of supersaturation on the growth rate $G(t)$. Setting $0 \leq j \leq 2$ in the optimization procedure (see Eq. 19) led to a preliminary estimation of the parameter vector θ with $j = 1.05$. The exponent $j = 1$ might be attributed either to a first order growth rate (e.g. linear part of Burton-Cabrera-Franck's growth model, as explained with Eq. (6)) or to prevailing diffusive limitation, but given the low viscosity of water and the high stirring rate set during the experiments, diffusive limitations around the growing particles are rather unlikely. The crystal growth rate was therefore assumed to be limited by a first-order integration mechanism and j was set to 1 in the following. The other estimated kinetic parameters are given in Table 1 (lines 1.1 and 1.2).

It is interesting to note that exponent $j = 2$ was previously reported by Mielniczek-Brzóska and Sangwal[53] for the growth of AO at low levels of supersaturation (i.e., $1.01 \leq \beta_{max} \leq 1.09$). However, according to the BCF model, this latter result does not prevent j from tending to 1 under higher levels of supersaturation. During this study, the maximum degree of supersaturation was higher: $1.1 \leq \beta_{max} \leq 1.2$, which could explain the shift of j.

The identification procedure was first tried using a set of experimental results straggling upon the whole range of operating conditions (i.e., with $5°C/h \leq dT/dt < 30°C/h$). It did not seem to be possible to converge toward a unique set of kinetic parameters. After analyzing the MSZW estimated from the concentration profiles, it appeared that two nucleation regimes were likely to take place, according to the cooling rate.[7] The kinetic identification was therefore performed after splitting the set of experiments in "slow" and "fast" cooling runs. Such an approach was successful and allowed to estimate two sets of kinetic parameters which are referred in the following to as "regime R_1" (line 1.1 in Table 1, for $dT/dt \geq 10°C/h$) and "regime R_2" (line 2.1 in Table 1, for $-30°C/h < dT/dt \leq 20°C/h$).

Without CSD data, accounting for the continuous generation of new particles through secondary nucleation was not necessary to represent the solute consumption. For both regimes, introducing Eq. 13 in addition to the primary nucleation expression (8) was useless as it did not allow improving the fit between the experimental and the simulated concentration trajectories. Figure 6 displays examples of model versus experimental results obtained without simulating secondary nucleation. The related predictions of the time variations of primary nucleation rates are also presented in Figure 5b. The second and third concentration curves related to both cooling rates -5 and -10°C are almost superimposed, even though

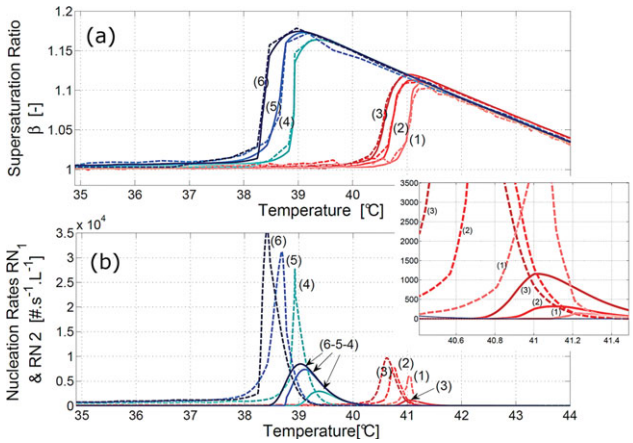

Figure 6. (a) Measured (dotted lines) and simulated evolutions of the supersaturation ratio β for six experiments performed with varying cooling rates: −5, −7, and −10°C/h (regime R_1) and −20, −25, and −30°C/h (regime R_2); (b) simulation of the variations of primary (solid line) and secondary nucleation rates (dotted line).

In inset: simulation of primary and secondary nucleation rates for regime R_1. [Color figure can be viewed in the online issue, which is available at wileyonlinelibrary. com.]

the simulated nucleation rates differ significantly (and consistently with theoretical consideration about the effect of the cooling rate on the intensity of primary nucleation).

For both regimes, the kinetic parameters were computed using simultaneously up to four model/experiments data sets feeding the optimization procedure. It is interesting to note, arguing from analogy with the theory of fluid mechanics, that the experimental results were not reproducible and exhibited erratic behaviors for intermediate cooling rates between −12 and −20°C/h. The crystallization mechanisms governing such "intermediate regime" would probably deserve to be more deeply investigated.

The optimal set of primary nucleation parameters corresponding to the simulation of the second crystallization regime R_2 is not fully satisfactory. Indeed, the simultaneous optimization of batch runs performed with $R \geq 20$°C/h did not allow reproducing satisfactorily the whole set of experimental data. As displayed in Figure 5, the simulated trajectory $C(t)$ is overestimated for $dT/dt = -25$°C/h, whereas it is underestimated for $dT/dt = -30$°C/h. The nucleation parameters seem therefore to result from a compromise, rather than from a satisfactory representation of the crystallization kinetics.

The modeling difficulties encountered in the case of regime R_2 suggest that the crystallization of AO at "high" cooling rates could involve more complex solid generation mechanisms than regime R_1. To analyze the differences observed between R_1 and R_2, the nucleation model for R_2 was assumed to be the result of primary homogeneous mechanisms generating a first population of particles, followed by secondary nucleation. Equation 13 was thus introduced in the computation of Eq. 17 giving the overall rate of nucleation R_N. Accounting for secondary nucleation mechanisms in the modeling of regime R_2 allowed to fit the set of experimental data with a much better accuracy than previously. Nevertheless, the obtained simulation results were not fully satisfactory and, in particular, did not allow consistent modeling of the CSD variations as a whole.

Parameter estimation based on both experimental solute concentration profiles and CSD data

As already mentioned, the CSD of the final particles was partially assessed using automatic off-line image analysis and human visual processing of the video pictures acquired during the crystallization experiments. Six examples of measured CSD histograms corresponding to six cooling crystallization processes are displayed in Figure 8. It is recalled that typical pictures of the growing crystals in suspension were also presented in Figure 1. Because of the wide range of operating conditions, one could expect the spreading of the CSD to increase significantly from low to high cooling rates. However, Figure 8 shows that even though the width of the CSD increases with the cooling rate, this increase remains moderate. This experimental observation suggests again that secondary nucleation could play a key-role during the whole crystallization process.

Now, a close observation of the in situ video pictures displayed in Figure 2a does not clearly allow conclusion about some noteworthy difference between the mechanisms of particle generation during R_1 and R_2. On the one hand, it seems that the fines content is slightly increased when the cooling rate is low. On the other hand, the scanning electronic microscopy (SEM) pictures displayed in Figure 2b show significant amounts of aggregated fine particles suggesting the onset of secondary nucleation during regime R_1.

To investigate more deeply, the nucleation mechanisms, the solute concentration measurements together with final CSD data were taken into account for the minimization of criterion (18). The estimation procedure yielded consistent simulation results. The related parameter estimates are presented in Table 1 where lines 2.1 and 2.2 give the estimated kinetic parameters for the two regimes R_1 and R_2. The confidence intervals are also displayed in Table 1. It can be seen that the two pre-exponential parameters A_{hom} and A_{SN} are much more uncertain than the growth rate constant k_g and the exponents i and k. In contradiction with the previous approach, it now clearly turns out that no satisfactory fit between the sets of experimental and simulated CSD data during R_1 could be obtained assuming a single primary nucleation mechanism. The introduction of secondary nucleation in the model turns out to be the only way of explaining the spreading of the measured CSD. Rather realistic particle sizes can now be predicted by the model, thanks to the simulation of prevailing secondary nucleation. Typical simulation results are thus displayed in Figures 8, curves 1 to 6.

Despite the rather poor quality of the CSD measurements, it seems reasonable to put forward that the results of the parameter estimation "have the ring of truth." First, because even though the identification was performed separately with two sets of experiments performed in regimes R_1 and R_2, the three parameters required by the expression of the secondary nucleation rate are unexpectedly identical. Second, because both the exponent and the growth rate constant resulting from the optimization procedure are almost equal. Indeed, according to the confidence intervals given in Table 1, the two estimated values of the growth rate constant (i.e., 2.56 and 2.74×10^{-5} m/s) can be considered as equal. This is quite consistent with the slight difference between the two CSD profiles displayed in Figure 9a, showing that given the lack of accurate CSD measurements, even 20% uncertainty about k_g does not change significantly the simulated CSD profiles. Indeed, Figure 9a shows two plots of CSDs

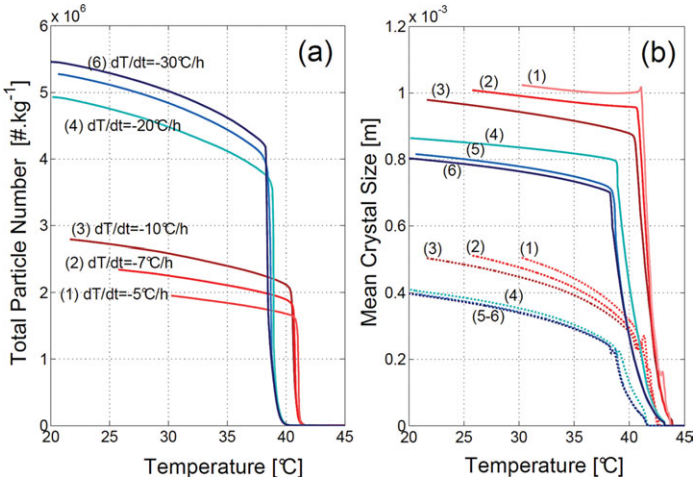

Figure 7. (a) Simulation of the overall number of particles generated during the batch operations displayed in Figure 6 and (b) Simulated number- and weight-average particle sizes (dotted and solid lines, respectively).

[Color figure can be viewed in the online issue, which is available at wileyonlinelibrary.com.]

simulated with $k_g = 20$ and 25 m/s during an experiment performed with the cooling rate $dT/dt = -7$°C/h (regime R_1). The two plots cannot really be considered as different.

Figure 7 displays the temperature variations of two important integral parameters computed from the simulated evolution of the CSD during the experiments presented in Figure 6. Consistently with the nucleation theory, the onset of the primary nucleation burst occurs at higher supersaturation levels when the cooling rate is increased, which increases the initial number of particles and, consequently, decreases the final average particle sizes.

Figure 8 shows the fit obtained between the experimental CSD data and the PBE simulation at the end of the batch process. The results are somewhat imperfect and deserve to be explained in more details. The performances of the image processing method used to characterize the particle sizes were reported to be rather encouraging.[50] Nevertheless, measuring automatically the CSD at the end of the process (i.e., with high solids content) remains quite difficult, due to the many overlapping particles. Moreover, the tremendous computation time required by the technique did not always allow satisfactory extraction of CSD estimates. As outlined earlier, due to the difficulties arising from the anisotropy of the particles, human visual expertise remained the best way of solving recognition problems which cannot easily be solved through automatic image processing. Such expertise is clearly a very tedious burden; this is the reason why the number of particles processed for reconstructing the CSD (i.e., 900–1000 particles) was rather limited and yield the poor and very noisy data displayed in Figure 8.

A second difficulty related to the use of the experimental CSD data arises from the reduced rangeability of the measured sizes, which was also outlined earlier. The very small particles do not appear in the video images, due to impossibility of seeing objects smaller than one pixel (2 μm). Even the particles with size up to 10 μm are blurred and many of these particles are masked by bigger crystals. Therefore, the estimated number of small particles cannot be considered as fully reliable. However, fitting the weight distribution rather

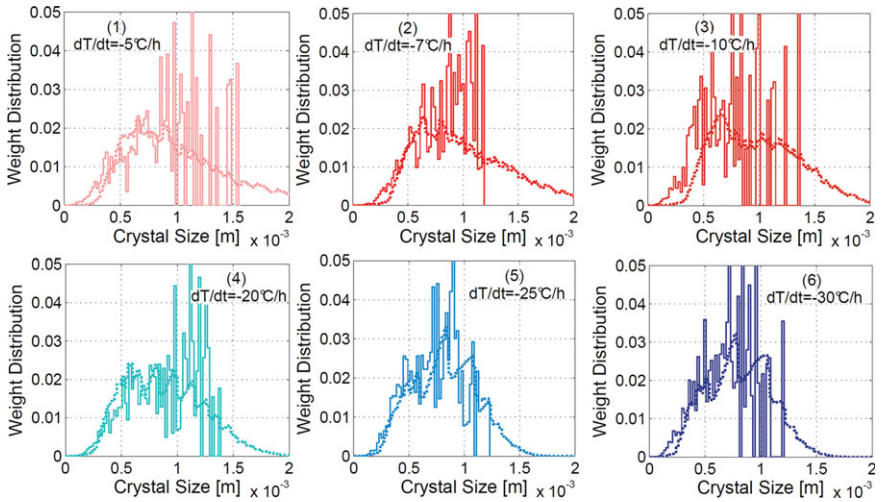

Figure 8. Comparison between the "measured" (bargraphs) and simulated (dotted lines) CSDs related to the batch operations displayed in Figure 6.

[Color figure can be viewed in the online issue, which is available at wileyonlinelibrary.com.]

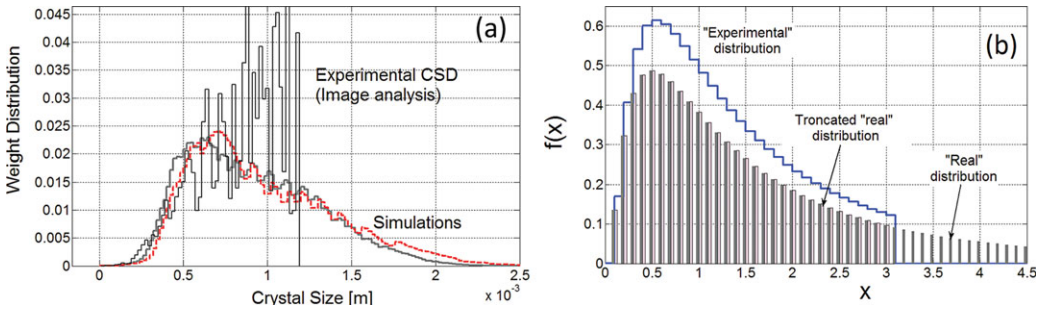

Figure 9. (a) Batch cooling experiment performed with $dT/dt = -7$°C/h; "measured" and simulated CSD.

Two simulations of the final CSD obtained with k_g=2.2 × 10^{-5} and 2.6 × 10^{-5} m/s show the sensitivity of the computed CSD to the growth rate parameter. (b) Effect of the truncation of lognormal CSD and overestimation of the fraction of modal sizes: it is simulated that particles larger than $x = 3$ cannot be measured. ($x > 3 \Leftrightarrow f(x) = 0$, with arbitrary units for x). [Color figure can be viewed in the online issue, which is available at wileyonlinelibrary.com.]

than the number distribution allowed getting round this problem because the contribution of small particles to the weight-CSD is thus negligible, as displayed in Figure 8.

In addition to the previous limitations, measuring particles exceeding 1–1.2 mm is clearly impossible, as explained earlier. One cannot therefore validate the model-predictions of the number fraction of the biggest particles in suspension. To cope with this latter difficulty, the criteria quantifying the mismatch between the simulated and measured CSD (i.e., the second part of Eq. 18) was computed inside the size bounds (25 and 110 μm), where the corresponding distribution functions were renormalized. Obviously, the two improvements brought to the computation of Eq. 18 cannot be considered as fully effective for solving adequately the difficulties raised by the poor quality of the video CSD measurements, but they clearly made the convergence of the optimization procedure much easier, and allowed obtaining the rather acceptable results which are displayed in Figure 8.

The simulation results presented in Figures 8 and 9 seem to underestimate the contribution of large particles to the overall CSD. It is clear that "renormalizing" the size distribution, when the right-hand side part of the distribution is missing, boils down to distort the experimental CSD in such a way that the modal size becomes overestimated. Figure 9b illustrates this point and shows that withdrawing the right-hand part of a lognormal distribution yields a distribution profile that can roughly be compared with the experimental results displayed in Figure 8.

Finally, it was also outlined earlier that the orientation of the elongated particles in the optical measurement cell leads to underestimate the real particle sizes. This problem cannot be considered as fully unpredictable because the flow of suspension in the measurement cell of the probe is likely to be oriented. However, reconstructing the real size distributions from the measured projected crystals would require a very significant modeling (e.g., CFD simulations) and mathematical work (i.e., reconstructing the true CSD from the measurements would require solving some complex inversion problem). Such a study was not performed during the present work.

The estimation of the growth rate parameters can also be discussed. As two different crystallization regimes were clearly identified, the steadiness of the crystal growth rate is rather unexpected: one could think that the transition from R_1 to R_2 corresponds to some change of growth mechanisms. For the same reasons, one could expect the secondary nucleation process to change with the rate at which supersaturation is generated. The opposite is shown by the model: the primary nucleation rate is found to be the only mechanism depending on the cooling rate while neither secondary nucleation nor crystal growth rates seem to differ during the transition from R_1 to R_2. SEM and atomic force microscopy (AFM) observations were performed to evaluate possible change of crystal surfaces or shapes, but these observations did not bring clear answers to the question.

Despite the undeniable coarseness and distortion of the CSD measurements, the model-predicted CSD profiles displayed in Figure 8 are all the same consistent with the experimental observations. It is clear that the CSD measurements bring essential quantitative information about the basic crystallization phenomena involved during the crystallization batch operations. Without such information, no reliable kinetic identification would have been obtained. In all honesty, the quality of the CSD analysis performed during this study is rather poor, but it is well-known that today the problem of measuring in-line the "true" CSD remains unsolved. For example, Ref. [3] was quoted earlier to provide valuable results and comments about the necessity of measuring the CSD for appropriate nucleation and growth parameter estimation. One could object however that the authors do not use true CSD measurements, but FBRM CLD experimental data (The FBRM probe yields chord length distribution, not CSD), which are known to give a distorted representation of real CSD. Despite the serious limitations of the FBRM the estimation results reported by Nagy et al.[3] are really interesting. It is reasonable to think that the same observation can be made about this study: even though the CSD computed using image processing is rather rough and approximate, the obtained experimental size data undeniably allow deeper analysis and quantitative kinetic identification of the nucleation mechanism is in question.

Figures 6 and 7 suggest that secondary nucleation occurs significantly for both high and low cooling rates. This point is also illustrated in Figure 10 where the prevalence of secondary nucleation is predicted to increase for decreasing cooling rates. According to the nucleation model (13) and using the parameters given in Table 1, two nucleation peaks can roughly be observed during the development of the batch process, but the discontinuity between the two phenomena is not clear-cut: one can see in Figure 7 that after reaching the maximal nucleation rate, a short period of decrease of primary nucleation is immediately followed by

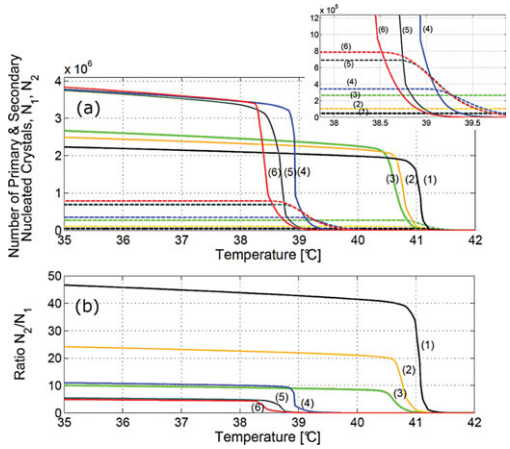

Figure 10. (a) Contribution of both primary (dashed lines) and secondary nucleation (solid lines) mechanisms to the overall generation of particles (N_1 and N_2 are the total numbers of particles generated through primary and secondary nucleation, respectively).

Inset: Magnification of the variations of the number of particles generated through primary nucleation. (b) Effect of the cooling rate on the prevalence of secondary nucleation. Indices (1)–(6) refer to increasing cooling rates from −5 to −30°C/h (see Figure 6). [Color figure can be viewed in the online issue, which is available at wileyonlinelibrary.com.]

an important increase of secondary nucleation. Then, the particle number increases sharply and reaches rapidly a "quasi steady-state" plateau, where few secondary particles are finally generated, due to the low level of supersaturation during the final cooling process.

Consistently with previous remarks, an interesting simulation result displayed in Figures 8 and 11 should also be outlined: the contribution of secondary nucleation to the overall generation of particles increases significantly when the cooling rate (i.e., the average level of supersaturation) decreases. The ratio between the number N_2 of particles issued from secondary nucleation, and the number of primary particles N_1 is given in Figure 11 at 35°C (= a temperature at which the solute concentration almost coincide with the solubility). This ratio is of the order of 10. This ratio results from differences in the nucleation processes displayed in Figure 10: the secondary nucleation rate is about six times higher than the primary nucleation rate when the cooling rate decreases from $dT/dt = -5$°C/h to $dT/dt = -30$°C/h. Moreover, it is interesting to note that Figure 11 underlines the transition between the two regimes. It can be seen that the PBE model predicts slight decrease of the ratio N_2/N_1 during regime R_2 for increasing cooling rates, whereas it predicts high but strongly decreasing values of the same ratio during regime R_1 when the cooling rate increases from −5 to −10°C/h. As far as process control is concerned, these observations have important consequences: it is usually assumed that reducing the cooling rate moderates the nucleation process and therefore reduces the spreading of the CSD. The results displayed in Figures 6 and 8 tend to weaken this assertion: even though the overall rate of nucleation increases with the rate of generation of supersaturation, the benefit of reduced primary nucleation is partially cut-down by the effects of secondary nucleation. The latter is therefore likely to reduce the efficiency of advanced temperature (and supersaturation) control strategies.

Conclusions

The dynamic modeling of the batch cooling solution crystallization of AO in water was developed using PBEs. The estimation of nucleation and growth parameters was performed using ATR-FTIR measurements of solute concentration and final CSD data computed from in situ video images of the crystallizing suspension. The PBE model allowed analyzing the respective contribution of supersaturation measurements and CSD data to the kinetic characterization of crystallization processes. In particular, the contributions and limitations of complementary sensing strategies to understanding and characterizing the nucleation and growth mechanisms were examined.

It can first be concluded that reliable evaluation and analysis of crystallization kinetics require measurements of both the continuous liquid phase and the solid dispersed phase. Even accurate continuous measurements of the solute concentration (which are not so frequently reported in the open literature) cannot be claimed to allow comprehensive estimation of the set of kinetic parameters involved during crystallization. Through the case-study presented here, it appears that the knowledge of the time variations of solute concentration allows, at best, evaluating a combination of parameters of the kinetic laws involved, but not their separate characterization. In particular, for simple primary nucleation and growth models, CSD data were demonstrated to be essential to resolve the entanglement of the nucleation and growth parameters. Even though the proposed mathematical demonstration is not claimed to cover any nucleation and growth kinetic situations, it is shown in Appendix that solute/solvent systems governed by simple kinetic laws like Eqs. 7 and 8 cannot be fully characterized using supersaturation data. However, the demonstration was only possible because the rate expressions (7) and (8) depend on the supersaturation profile only. Should the nucleation or growth rate expressions depend on other time-dependent variable (e.g., the overall solid concentration or area, the temperature, etc.), then the proof would no more be valid. In this latter case, it is likely that, paradoxically, very accurate measurements of solute concentration could allow identifying the nucleation and growth parameters.

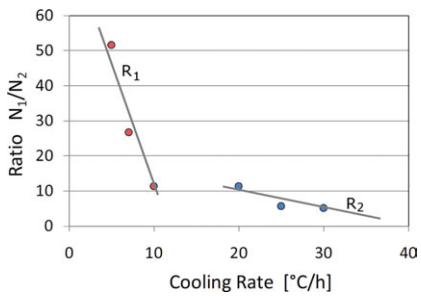

Figure 11. Values of the ratio between the numbers of primary and secondary particles: model-predictions at temperature T = 35°C against $R = -dT/dt$ (below 35°C, the supersaturation remains almost negligible).

[Color figure can be viewed in the online issue, which is available at wileyonlinelibrary.com.]

Second, despite the major restriction outlined earlier, the availability of accurate continuous supersaturation measurements allowed discriminating between possible nucleation mechanisms, even in the absence of CSD measurements. In this case-study, two crystallization regimes were thus observed, depending on the cooling rates. Nucleation phenomena occurring at higher cooling rates appeared to be more complex and more difficult to characterize than phenomena occurring at low cooling rate.

Third, thanks to both supersaturation and CSD measurements, the PBE simulation provides valuable understanding of the development of the crystallization process. Nucleation and growth kinetic parameters were thus estimated and the predictive features of the overall PBE model were found to be satisfactory. It seems reasonable to put forward that even really imperfect experimental CSD data can be highly valuable for kinetic estimation purposes. It was shown earlier that even incomplete, approximate, and noisy data allow designing a crystallization model which, in many ways, exhibits complex dynamic features.

Finally, as far as the AO/water crystallization system is concerned, several interesting points were observed and quantified. The cooling crystallization process turns out to be rather complex and raises many theoretical questions. It was shown in particular that the system is subject to two different kinetic regimes, depending on the cooling rate (i.e., the rate of generation of supersaturation). An intermediate irreproducible regime was also found to occur between the two previous ones. Such observation would deserve to be more deeply investigated.

Acknowledgments

We greatly acknowledge the French Research Agency ANR (Agence Nationale de la Recherche) for the support granted to the "white project" IPAPI (Improving the Properties of Active Pharmaceutical Ingredients), ref.07-BLAN-0183.

Literature Cited

1. Gimbun J, Nagy ZK, Rielly CD. Simultaneous quadrature method of moments for the solution of population balance equations, using a differential algebraic equation framework. *Ind Eng Chem Res*. 2009;48:7798–7812.
2. Aamir E, Nagy ZK, Rielly CD. Optimal seed recipe design for crystal size distribution control for batch cooling crystallisation processes. *Chem Eng Sci*. 2010;65:3602–3614.
3. Nagy ZK, Fujiwara M, Woo XY, Braatz RD. Determination of the kinetic parameters for the crystallization of paracetamol from water using metastable zone width experiments. *Ind Eng Chem Res*. 2008;47:1245–1252.
4. Nagy ZK. Model based robust control approach for batch crystallization product design. *Comput Chem Eng*. 2009;33:1685–1691.
5. Saengchan A, Kittisupakorn P, Paengjuntuek W, Arpornwichanop A. Improvement of batch crystallization control under uncertain kinetic parameters by model predictive control. *J Ind Eng Chem*., in press.
6. Borchert C, Ramkrishna D, Sundmacher K. *Model based prediction of crystal shape distributions. Proceeding of the 19th European Symposium on Computer Aided Process Engineering*. ESCAPE-19: June 14-17, 2009, Cracow, Poland. Vol. 26, 2009:141–146.
7. Gherras N, Févotte, G. Comparison between approaches for the experimental determination of metastable zone width: a case study of the batch cooling crystallization of ammonium oxalate in water. *J Crystal Growth*., in press.
8. Yu LX, Lionberger RA, Raw AS, D'Costa R, Wu H, Hussain AS. Applications of process analytical technology to crystallization processes. *Adv Drug Deliv Rev*. 2004;56:349–369.
9. Wu H, White M, Khan MA. Quality-by-Design (QbD): an integrated process analytical technology (PAT) approach for a dynamic pharmaceutical co-precipitation process characterization and process design space development. *Int J Pharm*. 2011;405:63–78.
10. Yu ZQ, Chew JW, Chow PS, Tan RBH. Recent advances in crystallization control: an industrial perspective. *Chem Eng Res Des*. 2007;85:893–905.
11. Leuenberger H, Lanz M. Pharmaceutical powder technology—from art to science: the challenge of the FDA's Process Analytical Technology initiative. *Adv Powder Technol*. 2005;16:3–25.
12. Nagy ZK, Chew JW, Fujiwara M, Braatz RD. Comparative performance of concentration and temperature controlled batch crystallizations. *J Process Control*. 2008;18:399–407.
13. Ma DL, Braatz RD. Robust identification and control of batch processes. *Comput Chem Eng*. 2003;27:1175–1184.
14. Chung SH, Ma DL, Braatz RD. Optimal model-based experimental design in batch crystallization. *Chemom Intell Lab Syst*. 2000;50:83–90.
15. Söhnel O, Mullin JW. Interpretation of crystallization induction periods. *J Colloid Interface Sci*. 1988;123:43–50.
16. Kashchiev D, Verdoes D, van Rosmalen GM. Induction time and metastability limit in new phase formation. *J Crystal Growth*. 1991;110:373–380.
17. Verdoes D, Kashchiev D, van Rosmalen GM. Determination of nucleation and growth rates from induction times in seeded and unseeded precipitation of calcium carbonate. *J Crystal Growth*. 1992;118:401–413.
18. Sangwal K. *Additives and Crystallization Processes*. Chichester, UK: Wiley, 2007.
19. Sangwal K. Kinetic effects of impurities on the growth of single crystals from solutions. *J Crystal Growth*. 1999;203:197–212.
20. Sangwal K. Growth kinetics and surface morphology of crystals grown from solutions: recent observations and their interpretations. *Prog Cryst Growth Char Mater*. 1998;36:163–248.
21. Sangwal K, Mielniczek-Brzóska E. Effect of cationic impurities on solubility and crystal growth processes of ammonium oxalate monohydrate: role of formation of metal-oxalate complexes. *Cryst Res Technol*. 2007;42:531–543.
22. Sangwal K, Mielniczek-Brzóska E. Effect of Cr(III) ions on the growth kinetics of ammonium oxalate monohydrate crystals from aqueous solutions. *J Cryst Growth*. 2002;242:421–434.
23. Sangwal K, Mielniczek-Brzóska E. Effect of Fe(III) ions on the growth kinetics of ammonium oxalate monohydrate crystals from aqueous solutions. *J Cryst Growth*. 2001;233:343–354.
24. Mielniczek-Brzoska E, Gielzak-Kocwin K, Sangwal K. Effect of Cu(II) ions on the growth of ammonium oxalate monohydrate crystals from aqueous solutions: growth kinetics, segregation coefficient and characterisation of incorporation sites. *J Cryst Growth*. 2000;212:532–542.
25. Lindenberg C, Mazzotti M. Effect of temperature on the nucleation kinetics of α l-glutamic acid. *J Cryst Growth*. 2009;311:1178–1184.
26. Ramkrishna D. *Population Balances: Theory and Applications to Particulate Systems in Engineering*. Waltham, MA: Academic Press, 2000.
27. Briesen H. Simulation of crystal size and shape by means of a reduced two-dimensional population balance model. *Chem Eng Sci*. 2006;61:104–112.
28. Sato K, Nagai H, Hasegawa K, Tomori K, Kramer, Jansens PJ. Two-dimensional population balance model with breakage of high aspect ratio crystals for batch crystallization. *Chem Eng Sci*. 2008;63:3271–3278.
29. Bajpai RK, Ramkrishna D, Prokop A. A coalescence redispersion model for drop-size distributions in an agitated vessel. *Chem Eng Sci*. 1976;31:913–920.
30. Mersmann A. Crystallization and precipitation. *Chem Eng Process*. 1999;38:345–353.
31. Sangwal K, Zdyb A, Chocyk D, Mielniczek-Brzóska E. Effect of supersaturation and temperature on the growth morphology of ammonium oxalate monohydrate crystals obtained from aqueous solutions. *Cryst Res Technol*. 1996;31:267–273.
32. Chernov AA. Notes on interface growth kinetics 50 years after Burton, Cabrera, and Frank. *J Cryst Growth*. 2004;264:499–518.
33. Burton WK, Cabrera N, Frank FC. The growth of crystals and the equilibrium structure of their surfaces. Philosophical transactions of the Royal Society of London. *Ser A Math Phys Sci*. 1951;243:299–358.
34. Mullin J. Allan S. Myerson, *Handbook of Industrial Crystallization*, 2nd ed. Waltham, MA: Butterworth-Heinemann, 2002.
35. Mullin JW. *Crystallization*, 3rd ed. London (UK): Butterworth-Heinemann, 1993.
36. Garside J, Larson M. Direct observation of secondary nuclei production. *J Cryst Growth*. 1978;43:694–704.

37. Févotte F, Févotte G. A method of characteristics for solving population balance equations (PBE) describing the adsorption of impurities during crystallization processes. *Chem Eng Sci*. 2010;65:3191–3198.
38. Togkalidou T, Fujiwara M, Patel S, Braatz RD. Solute concentration prediction using chemometrics and ATR-FTIR spectroscopy. *J Cryst Growth*. 2001;231:534–543.
39. Pöllänen K, Häkkinen A, Reinikainen S-P, Rantanen J, Karjalainen M, Louhi-Kultanen M, Nystrom L. IR spectroscopy together with multivariate data analysis as a process analytical tool for in-line monitoring of crystallization process and solid-state analysis of crystalline product. *J Pharm Biomed Anal*. 2005;38:275–284.
40. Lewiner F, Klein JP, Puel F, Févotte G. On-line ATR FTIR measurement of supersaturation during solution crystallization processes. Calibration and applications on three solute/solvent systems. *Chem Eng Sci*. 2001;56:2069–2084.
41. Scholl J, Bonalumi D, Vicum L, Mazzotti M, Muller M. In situ monitoring and modeling of the solvent-mediated polymorphic transformation of L-glutamic acid. *Cryst Growth Des*. 2006;6:881–891.
42. Presles B, Debayle J, Févotte G, Pinoli J-C. Novel image analysis method for in situ monitoring the particle size distribution of batch crystallization processes. *J Electron Imaging*. 2010;19:1–7.
43. Févotte G. New perspectives for the on-line monitoring of pharmaceutical crystallization processes using in situ infrared spectroscopy. *Int J Pharm*. 2002;241:263–278.
44. Presles B, Debayle J, Rivoire A, Févotte G, Pinoli J-C. Monitoring the particle size distribution using image analysis during batch crystallization processes. Proceedings 9th SPIE Internat. Conference on Quality Control by Artificial Vision (QCAV), Wels, Austria, May 2009.
45. Eggers J, Kempkes M, Cornel J, Mazzotti M, Koschinski I, Verdurand E. Monitoring size and shape during cooling crystallization of ascorbic acid. *Chem Eng Sci*. 2009;64:163–171.
46. Kempkes M, Vetter T, Mazzotti M. Measurement of 3D particle size distributions by stereoscopic imaging. *Chem Eng Sci*. 2010;65:1362–1373.
47. Kempkes M, Vetter T, Mazzotti M. Monitoring the particle size and shape in the crystallization of paracetamol from water. *Chem Eng Res Des*. 2010;88:447–454.
48. Simon LL, Nagy ZK, Hungerbuhler K. Endoscopy-based in situ bulk video imaging of batch crystallization processes. *Org Process Res Dev*. 2009;13:1254–1261.
49. Zhou Y, Srinivasan R, Lakshminarayanan S. Critical evaluation of image processing approaches for real-time crystal size measurements. *Comput Chem Eng*. 2009;33:1022–1035.
50. Ahmad O, Debayle J, Gherras N, Presles B, Févotte G, Pinoli JC. Recognizing overlapped particles during a crystallization process from in situ video images for measuring their size distributions. 2011. ISIC'18, 18th International Conference on Industrial Crystallization, Zurich, 13–16 September, 2011.
51. Nyvlt J. Nucleation and growth rate in mass crystallization. *Prog Cryst Growth Charact Mater*. 1984;9:335–370.
52. Kim KJ, Mersmann A. Estimation of metastable zone width in different nucleation processes. *Chem Eng Sci*. 2001;56:2315–2324.
53. Mielniczek-Brzóska E, Sangwal K. Study of growth kinetics of ammonium oxalate monohydrate crystals from aqueous solutions. *Cryst Res Technol*. 1994;29:1027–1035.

Appendix

The solid concentration $C_s(t)$ is computed after integrating the whole set of particles in suspension at time t. Denoting by v(L) the volume of one single particle of size L, ϕ_v its volumetric shape factor ($\pi/6$ for spherical crystals), and ρ_S the specific mass of AO, one can write

$$v(L,t) = \phi_v L(t)^3 \quad \Rightarrow \quad m(L,t) = \rho_s \phi_v L(t)^3 \tag{A1}$$

Therefore, after integration of the set of size-distributed particles and referring the PDF ψ (L,t) [in (# m^{-1} s^{-1}) m^{-3}] to 1 unit volume of suspension

$$C_s(t) = m_{\text{Total}}(t) = \rho_s \phi_s \int_0^{L_{\max}} \psi(L,t)\, L(t)^3 dL \tag{A2}$$

Whatever the kinetic expression of the growth rate, one can generally write $G(t) = k_g\, g(\beta(t)) = dL/dt$, where $g(\beta(t))$ represents the effect of supersaturation $\beta(t)$ on the crystal growth rate [e.g., $g = \beta + 1$, $g = (\beta + 1)^2$] and k_g is the growth rate constant (m/s).

It follows that

$$C_s(t) = \rho_s \phi_s \int_0^{L_{\max}} \psi(L,t)\, L(t)^3 dL = \rho_s \phi_s \int_0^{L_{\max}} \psi(L,t) \left[\int_v^t G(\tau)\, d\tau\right]^3 dL \tag{A3}$$

where $v(L,t)$ is the nucleation time of the particles with size $L(t)$.

The PDF is defined as $\psi(L,t) = \frac{n(L,t)}{\mathrm{dL}} = \frac{R_N(t)\, dt}{dL} \Rightarrow \psi(L,t)\, dL = A.n(t)\, dt$, where parameter A is here considered as constant and n ($\beta(t)$) depends on supersaturation only (e.g., $n = \exp\left(\frac{-B}{(\ln \beta)^2}\right)$).

The following expression of C_s is obtained, where t_{fin} is the final batch time

$$C_s(t) = A\, \rho_s \varphi_s \int_0^{t_{\text{fin}}} n(\beta(t))\, dt \left[\int_v^t k_g\, g(\beta(\tau))\, d\tau\right]^3$$
$$= k_g^3 A \rho_s \varphi_s \int_0^{t_{\text{fin}}} n(\beta(t)) \left[\int_v^t g(\beta(\tau))\, d\tau\right]^3 dt = k_g^3 A\, \rho_s \varphi_s\, \chi(\beta(t)) \tag{A4}$$

The goal is to estimate A and k_g from measured concentration profiles, the time functions $\beta(t)$ and $C_s(t)$ are thus derived from fixed experimental data such that the following ratio χ ($\beta(t)$) is constant

$$\chi(\beta(t)) = \frac{C_s(t)}{\rho_s \varphi_s \int_0^{t_{\text{fin}}} n(\beta(t)) \left[\int_v^t g(\beta(\tau))\, d\tau\right]^3 dt} = k_g^3 A \tag{A5}$$

The product $k_g{}^3$ A is therefore constant for given nucleation and growth expressions and experimental solute concentration trajectory $C(t)$. Consequently, measuring $C(t)$ yields $k_g{}^3$ A, and does not allow estimating separately k_g and A.

Manuscript received Feb. 9, 2011, revision received July 23, 2011, and final revision received Sept. 9, 2011.